

Article

Dynamic Mechanical Behavior and Energy Release Effect of a Novel Nb₁₇Zr₃₃Ti₁₇W₃₃ High-Entropy Alloy under Impact Load

Wensu Ji ^{1,2} , Qiang Zou ^{1,*}, Xiaoyun Yin ¹ and Zhengwang Zhu ^{3,*}¹ Naval University of Engineering, Wuhan 430033, China² Ordnance Non-Commissioned Officers School, Army Engineering University of PLA, Wuhan 430075, China³ School of Metallurgy, Northeastern University, Shenyang 110819, China

* Correspondence: 13256903326@163.com (Q.Z.); zhzw@mail.neu.edu.cn (Z.Z.)

Abstract: The present study successfully demonstrates the fabrication of a novel class of high-entropy alloy, namely Nb₁₇Zr₃₃Ti₁₇W₃₃, through suspension melting and casting technique. To investigate the dynamic mechanical behavior and energy release effects of the alloy under high-speed impact loads, various techniques were employed, including split Hopkinson pressure bar (SHPB), X-ray diffractometer (XRD), scanning electron microscope (SEM), and high-speed photography. These methods were utilized to acquire crucial data, such as crystal structure analysis, stress–strain curves, and microstructural examination of failed specimens. The modified Johnson–Cook (J-C) model was employed to elucidate the dynamic flow behavior of the alloy, while investigating the failure mechanism and energy release phenomenon during the process of dynamic compression. The experimental results demonstrate that the alloy material exhibits a dual-phase (BCC1 + BCC2) structure, exhibiting ductile fracture behavior under dynamic compression conditions. On the fracture surface, typical dimple structures along with evidence of shear slip and melting traces were observed, indicating an energy-releasing failure process. The newly developed alloy exhibited exceptional strength, high density, remarkable plasticity, and outstanding energy release properties, rendering it highly promising for applications under extreme loads.



Citation: Ji, W.; Zou, Q.; Yin, X.; Zhu, Z. Dynamic Mechanical Behavior and Energy Release Effect of a Novel Nb₁₇Zr₃₃Ti₁₇W₃₃ High-Entropy Alloy under Impact Load. *Metals* **2023**, *13*, 2013. <https://doi.org/10.3390/met13122013>

Academic Editors: Yong Zhang, Giuseppe Lacidogna and Jiro Kitagawa

Received: 9 September 2023

Revised: 25 October 2023

Accepted: 12 December 2023

Published: 15 December 2023



Copyright: © 2023 by the authors. Licensee MDPI, Basel, Switzerland. This article is an open access article distributed under the terms and conditions of the Creative Commons Attribution (CC BY) license (<https://creativecommons.org/licenses/by/4.0/>).

Keywords: high-entropy alloy; impact load; failure mechanism; constitutive relation

1. Introduction

High-entropy alloys break through traditional alloy design concepts and are typically composed of a mixture of four or more elements with equal or near equal molar ratios [1,2]. The high-entropy effect significantly reduces the Gibbs free energy [3], thereby inhibiting the formation of intermetallic compounds and complex phases. Instead, it facilitates the formation of simple solid-solution structures and exhibits exceptional physical and mechanical properties, including high strength, hardness, toughness, friction resistance, fatigue resistance, and corrosion resistance, which have been extensively studied and applied both domestically and internationally [4–6]. In particular, the refractory high-entropy alloy systems comprising Zr, W, V, Ti, Ta, Nb, Mo, Hf, and Cr exhibit distinctive physical and mechanical properties as well as energy release effects that render them promising candidates for the special equipments application [7,8].

At present, the majority of investigations on the mechanical properties of high-entropy alloys primarily focus on quasi-static loading conditions, where the loading rate is usually between 10^{-4} s^{-1} and 10^{-2} s^{-1} , with limited attention being given to their response under high-speed dynamic loading. The Ti₃₀(TaNbZr)₆₀Mo₁₀ high-entropy alloy was designed and synthesized by Li et al. using first-principles calculations [9]. The quasi-static compression test revealed a yield strength of 1132 MPa and a plastic strain of 33%. Comparative analysis with the equiatomic ratio TiTaNbZrMo alloy experiment demonstrated superior overall mechanical properties. The refractory high-entropy alloys, Nb₂₅Mo₂₅Ta₂₅W₂₅ and

$V_{20}Nb_{20}Mo_{20}Ta_{20}W_{20}$, were prepared by O.N. Senkov et al. using vacuum arc melting technology [10]. The flow characteristics and microstructure evolution rules of these two alloys under quasi-static compression were investigated. They found that both alloys had a single-phase body-centered cubic (BCC) structure and showed extensive compressive plastic strain at 600 °C and above. NbMoTaW refractory high-entropy alloy films with super ductility were prepared by Yu et al. [11] using magnetron sputtering technology. He et al. [12] reported a novel $Re_{0.1}Hf_{0.25}NbTaW_{0.4}C_{0.25}$ refractory high-entropy alloy (RHEA) with both excellent high-temperature strength and decent room-temperature ductility. The alloy exhibited an excellent compressive strength of 1026 MPa at 1450 °C and 523 MPa at 1700 °C, with a good compressive fracture strain of 10.2% at room temperature, which has potential applications in the field of ultra-high temperature structural materials. Guo et al. [13] analyzed the competition and balance mechanism between work hardening resulting from the surge in dislocations and material softening caused by plastic deformation during contact loading in $Al_{0.3}CoCrFeNi$ high-entropy alloy. They found that dislocation tangles and twin boundaries hinder dislocation motion, lead to work hardening, also free dislocation glide and annihilation, as well as the formation of steps and the partial slip, where the slip plane and Burgers vector are parallel to the twin boundary, result in materials softening. However, it is important to note that the special equipments application of high-entropy alloys involves a dynamic and evolving service environment rather than a static one. Additionally, they are frequently exposed to sudden impact loads, such as axial recoil during projectile launch, high-speed impact upon target penetration, and explosive impact. Therefore, investigating the mechanical properties under high-speed dynamic loads is advantageous for materials to effectively respond to unforeseen events during complex operational processes and fully exploit the potential mechanical benefits of high-entropy alloys. The effect of the strain rate on the dynamic mechanical properties of $AlCrCuFeNi_2$ high-entropy alloy was investigated by Ma et al. [14]. It was observed that the dynamic yield strength exhibited a linear relationship with the strain rate, accompanied by a significant enhancement in the strain hardening rate under dynamic loading. Li et al. [15] investigated the dynamic response and microstructure evolution of a single-phase (FCC) $Al_{0.3}CoCrFeNi$ high-entropy alloy under high strain rates, revealing its exceptional strain hardening ability that contributes to a remarkable shear failure resistance. These findings suggest that this alloy holds promise as a potential material for applications requiring penetration protection, such as armor.

The Hopkinson compression test, in addition to its advantage of testing the dynamic mechanical properties of materials, eliminates the need for wave effects consideration in sample deformation analysis. The stress wave effect and strain rate effect have been effectively decoupled to accurately determine the mechanical properties of materials under high strain rates. It is the main experimental method for studying the internal force behavior of materials in a strain rate ranging from 10^2 s^{-1} to 10^4 s^{-1} . In order to replace traditional inert materials (steel, tungsten, copper, etc.) in special equipments, our research group successfully pioneered the development of a groundbreaking high-density energetic structural material—the $Nb_{17}Zr_{33}Ti_{17}W_{33}$ high-entropy alloy. This proportion of alloy (a molar ratio of 1:2:1:2) has not been reported before. Additionally, the dynamic mechanical properties, failure mechanism, and energy release mechanism of the $Nb_{17}Zr_{33}Ti_{17}W_{33}$ high-entropy alloy under impact loading were investigated using split Hopkinson pressure bar (SHPB), scanning electron microscope (SEM), X-ray diffractometer (XRD), and high-speed photography. The dynamic constitutive relationship was further established. The purpose of this study is to conduct preliminary work on the application of the $Nb_{17}Zr_{33}Ti_{17}W_{33}$ high-entropy alloy in special equipments by assessing the mechanical behavior and the energy release effect under high-speed impact loads.

2. Materials and Methods

2.1. Alloy Preparation

$\text{Nb}_{17}\text{Zr}_{33}\text{Ti}_{17}\text{W}_{33}$ alloy ingots (with each element in a molar ratio of 1:2:1:2) were prepared using industrial-grade Nb, Zr, Ti, and W raw materials (>99.9 wt.% purity) through suspension melting casting technology under the protection of a high-purity argon atmosphere (99.99 mass%). To ensure component element uniformity, the prepared masterbatch underwent a repeated process of flipping and melting for at least 5 cycles, with each cycle maintaining a liquid state for approximately 30 min. The preparation procedure is illustrated in Figure 1. The density of the alloy materials measured by the Archimedes drainage method was $10.98 \text{ g}\cdot\text{cm}^{-3}$.

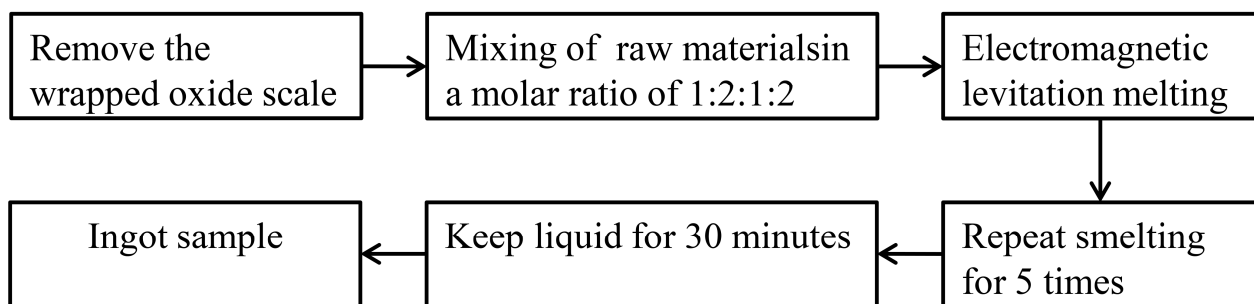


Figure 1. Preparation process flow.

2.2. Test Methods

The $18 \text{ mm} \times 2 \text{ mm}$ cylindrical sample was taken from the master ingot, and the upper and lower surfaces were polished to analyze the phase structure composition of the alloy by XRD (Rigaku Dmax 2500, Rigaku Corporation, Tokyo, Japan). The experimental conditions included a tube voltage of 50 kV, tube current of 50 mA, scanning angle range from 20 to 90° with a scanning speed of $6^\circ/\text{min}$, and a scanning step size of 0.02. The microstructure and fracture morphology of the alloy were examined using SEM (JSM-7100F, Japan Electronics, Tokyo, Japan) following dynamic compression, while the elemental distribution within each phase was analyzed utilizing an energy dispersive spectrometer (EDS).

The impact strain rate ranges from 10^2 s^{-1} to 10^4 s^{-1} when employing SHPB for room-temperature dynamic impact testing. The operational principle involves the air gun firing high-speed bullets to impact the input rod, which in turn strikes the sample and causes deformation. This effect is then transmitted under pressure to the output rod, while also hitting the cache device via an absorption rod. Throughout this process, one-dimensional elastic stress waves are incident, reflected, and transmitted. The three actions were recorded as pulse signals using a highly sensitive strain gauge, capturing essential data, such as loading rate and stress waveform. These signals were then meticulously logged by a computer system. Ultimately, the material's dynamic stress–strain curve under high-speed load was generated through an advanced data-processing system and an intelligent measurement analyzer. The arrangement of the pressure rod, specimen, and test instrument is illustrated in Figure 2. As a comparison, a quasi-static compression test was conducted by an electronic universal material testing machine with a strain rate of 10^{-3} s^{-1} . The compressed sample was obtained from an alloy ingot through wire cutting. The quasi-static test sample measured $6 \text{ mm} \times \Phi 4 \text{ mm}$, while the dynamic test sample measured $4 \text{ mm} \times \Phi 4 \text{ mm}$.

Based on the results of the uniaxial compression mechanical performance tests, the mechanical model of the material was solved, the damage and destruction process of the material were observed, and the failure and energy release mechanism of the material were analyzed.

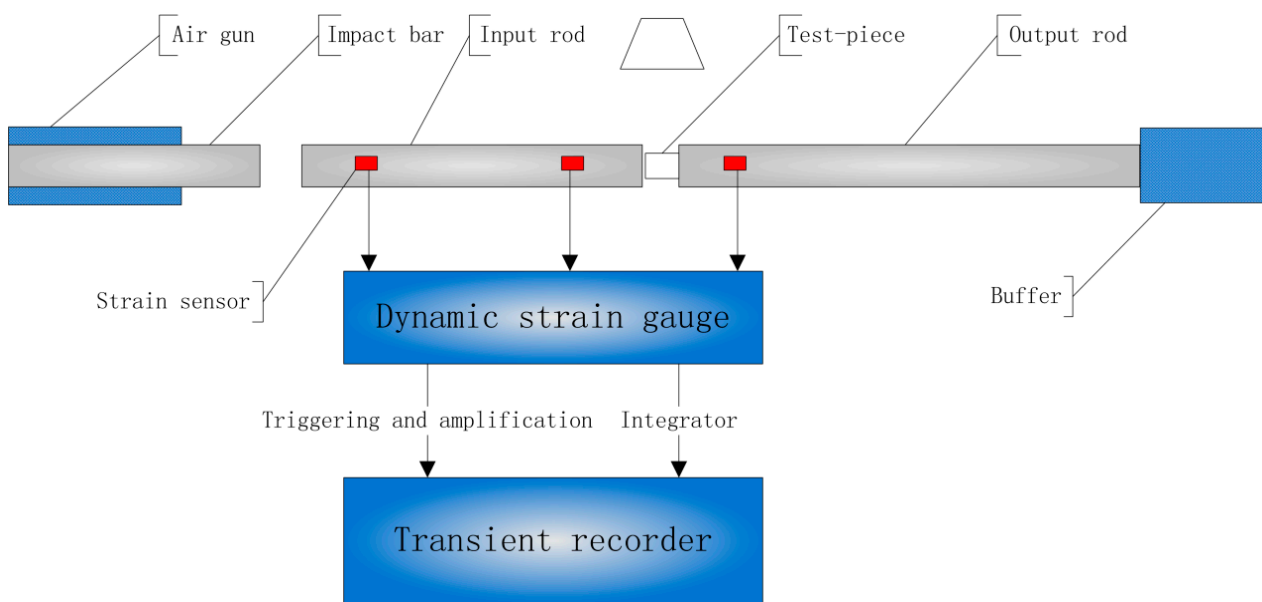


Figure 2. Schematic diagram of the SHPB test facility.

3. Results and Discussion

3.1. Alloy Crystal Structure

The XRD pattern of the $\text{Nb}_{17}\text{Zr}_{33}\text{Ti}_{17}\text{W}_{33}$ alloy sample is depicted in Figure 3. The results reveal the presence of a body-centered cubic structure (BCC) in the alloy, with no other complex phases being observed. The high mixing entropy effect of the alloy contributes to the enhanced compatibility of its main components, leading to a significant reduction in the system's free energy and consequently suppressing element segregation trends. When the mixing entropy of the system surpasses the entropy change associated with intermetallic compound formation, it can effectively suppress the occurrence of brittle intermetallic compounds and promote the formation of simple solid solutions. The analysis revealed that the $\text{Nb}_{17}\text{Zr}_{33}\text{Ti}_{17}\text{W}_{33}$ alloy sample exhibits a dual-phase composition, comprising two distinct body-centered cubic structures, namely, BCC1 and BCC2 phases. Shen et al. [16] demonstrated that the presence of tungsten in alloys promotes phase separation, which aligns with the observed phenomenon in this study. The lattice constants corresponding to BCC1 and BCC2 are 3.195 Å and 3.484 Å, respectively. The plane (110) of the alloy exhibits a significantly higher diffraction intensity, indicating a distinct preferred growth orientation. Conversely, the diffraction peak intensity diminishes at larger angles due to variations in atomic sizes and a significant lattice distortion inherent in multi-principal-component high-entropy alloys. Consequently, an increase in the angle results in enhanced slow scattering effects.

The equilibrium solidification microstructure of the $\text{Nb}_{17}\text{Zr}_{33}\text{Ti}_{17}\text{W}_{33}$ high-entropy alloy in its cast state is illustrated in Figure 4. A microzone EDS analysis was conducted on the bright white and black-gray regions, with the corresponding results being presented in Figure 5. The equilibrium solidified state of the alloy exhibits two distinct types of segregation, as depicted in Figure 4. The bright body exhibits a high enrichment of W element (Figure 5a), with a remarkable content reaching up to 72.5 at.%, while the presence of other elements is significantly limited. The black gray body exhibits an enrichment of the Zr element (Figure 5b), with a composition of 54.7 at.%. The elements Ti and Nb exhibit a dendritic morphology in both phases, displaying a relatively homogeneous distribution. The mixing enthalpies between the W and Ti, Zr, and Nb elements exhibit negative values of -6 , -9 , and -8 kJ/mol, respectively. The insufficient mixing entropy between the elements fails to counterbalance the negative mixing enthalpy, and additionally, W ($T_m = 3422$ °C) has a significant difference in melting point compared to other elements, resulting in limited miscibility between W and the other elements. During the solidification process, the W

element is incorporated into the dendrites, ultimately resulting in a solid-solution structure that exhibits an enrichment of the W element. The W-rich bright body corresponds to the BCC1 phase due to its smaller lattice constant compared to that of the gray BCC2 phase. The obtained results are in excellent accordance with our deliberate composition design aimed at achieving a simplified solid-solution structure of $\text{Nb}_{17}\text{Zr}_{33}\text{Ti}_{17}\text{W}_{33}$.

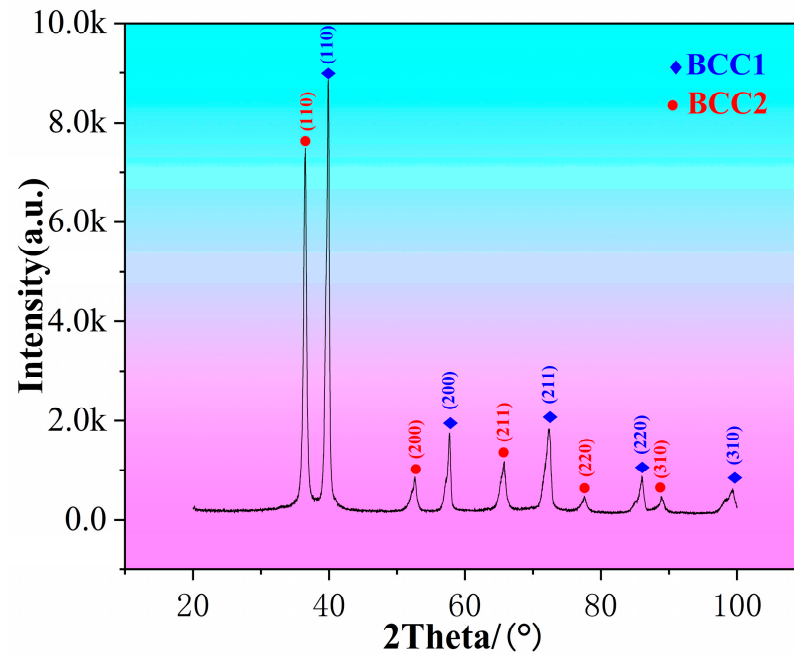


Figure 3. XRD patterns of the $\text{Nb}_{17}\text{Zr}_{33}\text{Ti}_{17}\text{W}_{33}$ high-entropy alloy.

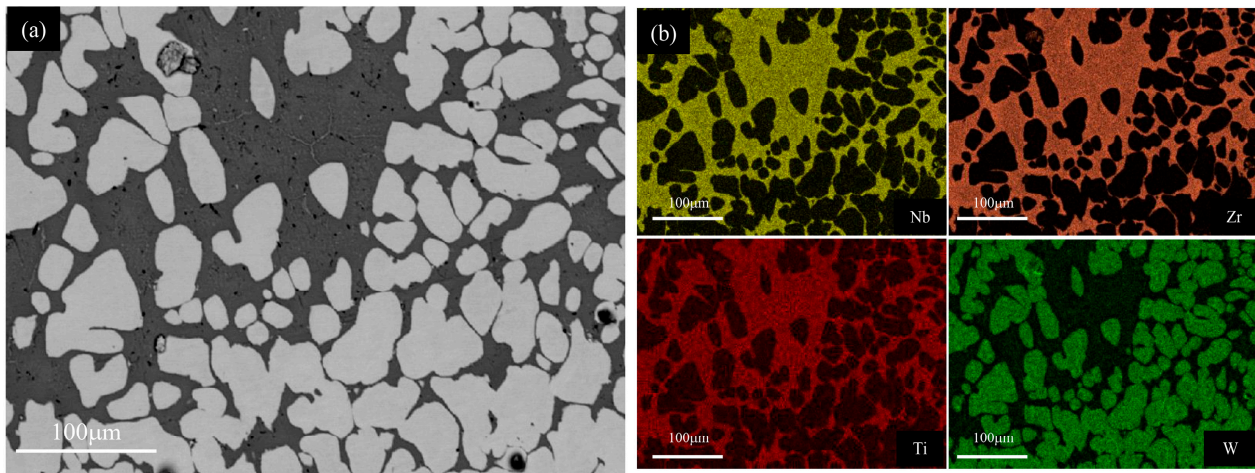


Figure 4. Microstructure (a) and EDS surface scanning results (b) of the $\text{Nb}_{17}\text{Zr}_{33}\text{Ti}_{17}\text{W}_{33}$ high-entropy alloy.

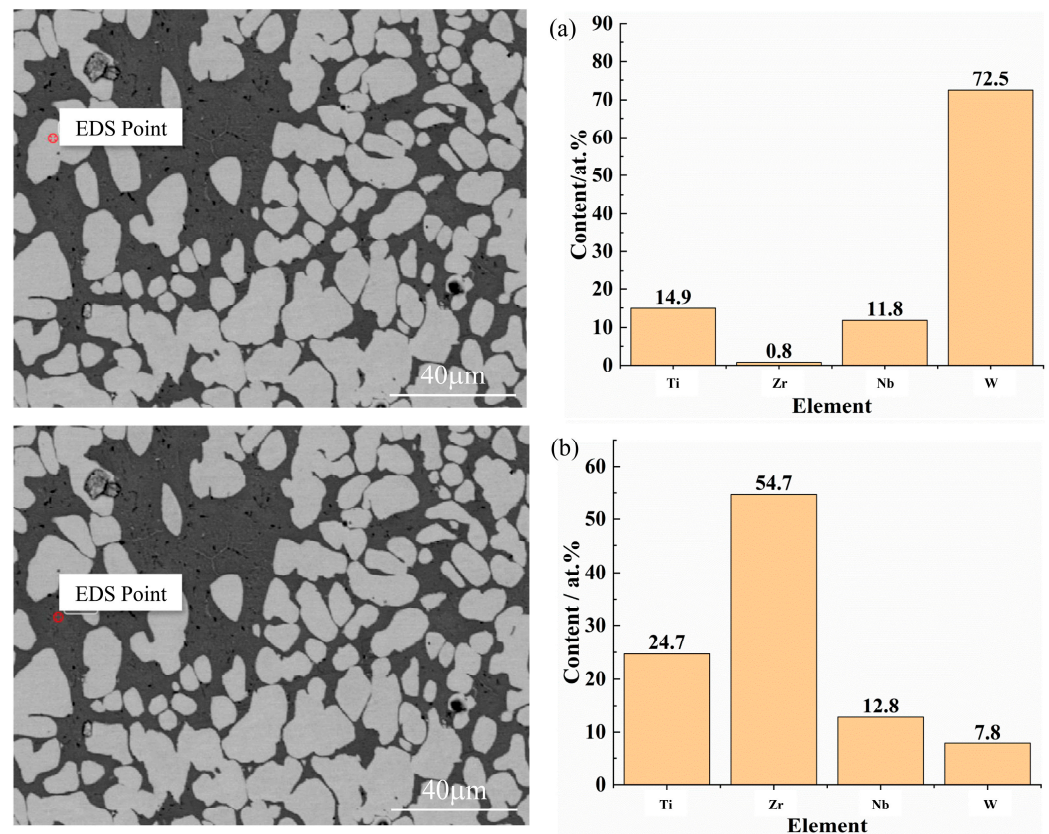


Figure 5. Scanning images and energy spectrum analysis results of the bright area (a) and dark area (b).

3.2. Strain Rate Effect

The engineering stress–strain curve obtained from the unidirectional compression test elucidates the dynamic deformation and fracture behavior of the alloy, as depicted in Figure 6. The observed phenomenon of strain rate hardening is significant: as the initial strain rate increases from 0.001 to 4294 s^{−1}, there is an increase in dynamic yield strength from 965 to 1587 MPa, and an increase in compressive strength from 1300 to 1772 MPa. The positive strain rate effect facilitates an enhanced energy absorption during high-speed deformation, thereby promoting the subsequent energy release phenomenon. The sample exhibited coarseness at strain rates of 808 and 1359 s^{−1}, while cracks appeared at a higher strain rate of 2494 s^{−1} without complete fracture. Upon reaching a strain rate of 3689 s^{−1}, the specimen experienced complete fracture, exhibiting a fracture strength of 1683 MPa and a fracture strain of 27.32%. The alloy exhibits remarkable strength and plasticity at such a high strain rate, surpassing the majority of high-entropy alloy systems with either FCC or BCC structures in terms of comprehensive mechanical properties [17]. The dynamic stress–strain curve of the sample exhibits a significant disparity with the smooth deformation curve observed during quasi-static loading. In contrast to the smooth deformation curve observed under quasi-static loading, dynamic impact induces a slight decrease in stress after reaching the yield point, followed by entry into the plastic deformation stage characterized by “serrated” fluctuations in stress. The stress rapidly decreases upon reaching its maximum value. The fracture failure of the alloy occurs at a strain level of approximately 38% under static loading, which is about 1.5 times higher than the strain at which dynamic compression failure occurs. The significant disparity between the two arises from the coexistence of strain strengthening induced by the dislocation and thermal softening effect caused by the adiabatic temperature rise during dynamic compression, resulting in a localized temperature elevation and diminished material plasticity. Several scholarly

publications [18–20] describe this dynamic failure mechanism as adiabatic shear failure resulting from thermo-mechanical instability.

The response of the yield limit to the strain rate is depicted in Figure 7 under quasi-static and dynamic loading conditions, illustrating two distinct regions denoted as Zone I and Zone II. A conclusion can be inferred that the yield limit of the alloy material exhibits an increasing trend with the augmentation of the strain rate Region I representing the response at low strain rates, where the yield limit can be regarded as a constant. The influence of the strain rate is negligible, whereas Region II demonstrates that the flow stress exhibits a high sensitivity to changes in the strain rate. According to the Von Mises theory, a parameter sensitive to the strain rate can be derived as follows:

$$\lambda = \left. \frac{\partial \sigma}{\partial \log \dot{\varepsilon}_p} \right|_{T, \varepsilon_p}, \quad (1)$$

where σ and $\dot{\varepsilon}_p$ are the stress and strain rates, respectively. λ corresponds to the linear fitting slopes of the low strain-rate Region I and high strain-rate Region II in Figure 7, denoted as λ_I and λ_{II} , respectively. The strain rate sensitivity coefficients of the alloy can be obtained from Formula (1) as $\lambda_I = 36.0$ and $\lambda_{II} = 444.4$, respectively. The strain rate sensitivity of high-entropy alloys under dynamic conditions is much higher than that under quasi-static loading, which may be due to different thermal excitation mechanisms under the two conditions. The excited free energy ΔG represents certain energy barriers that need to be crossed to overcome dislocation interference. It is generally believed that the relationship between ΔG and strain rate $\dot{\varepsilon}_p$ is as follows [21]:

$$T = \frac{-\Delta G}{K} (\tau^*, T) \left[\ln \frac{\dot{\varepsilon}_p}{\dot{\varepsilon}_0} \right]^{-1}, \quad (2)$$

where ΔG is the free energy of excitation, which is a function of local thermal stress τ^* and adiabatic temperature T ; $\dot{\varepsilon}_0$ is the reference strain rate, depending on the structural state of the material function; and K is a constant under certain stress and strain rate conditions.

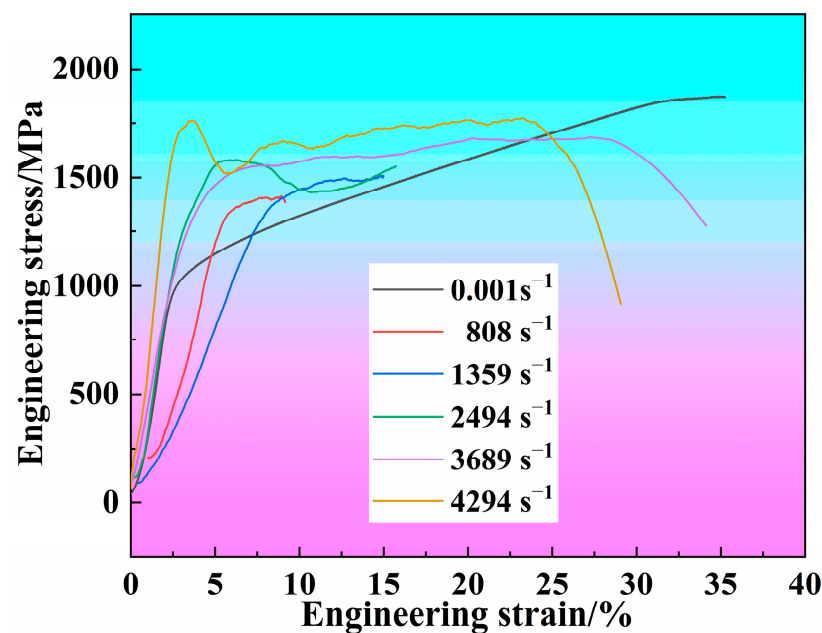


Figure 6. Engineering stress–strain curves of the Nb₁₇Zr₃₃Ti₁₇W₃₃ high-entropy alloy at various strain rates.

According to Formula (2), when the variation of the absolute temperature T and $\dot{\varepsilon}_0$ are not significant, the thermal excitation free energy is inversely proportional to the strain rate. For the low strain-rate Region I, the mechanism controlling the plastic flow is frictional stress [22]. A significant quantity of precipitates is observed within the lattice, accompanied by a high thermal excitation free energy. The thermal lattice vibrations are insufficient to overcome these obstacles, and the yield limit remains unaffected by the applied strain rate. Therefore, the yield limit exhibits a greater sensitivity to the strain rate. It has been observed that materials possessing a body-centered cubic crystal structure display a comparable strain rate sensitivity, such as annealed uranium and annealed low-carbon steel [23,24].

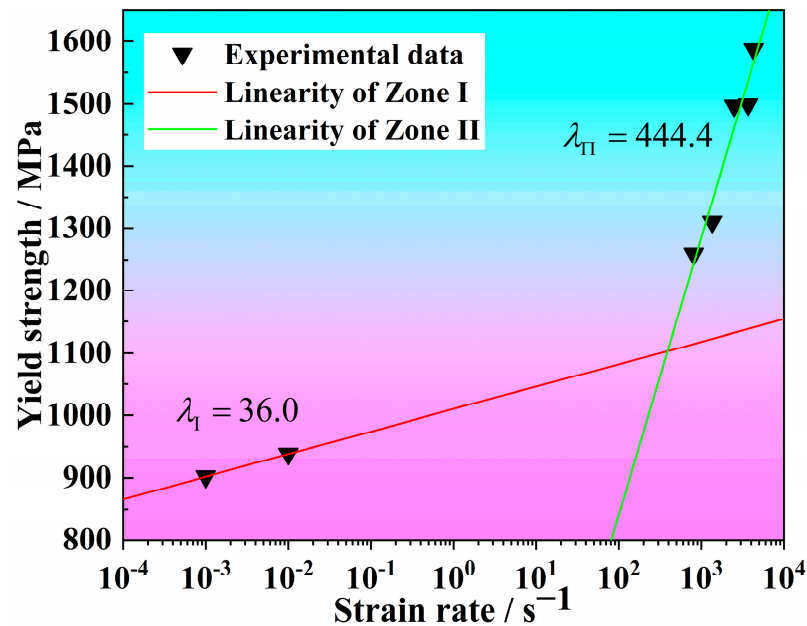


Figure 7. Strain rate sensitivity of the yield strength for the Nb₁₇Zr₃₃Ti₁₇W₃₃ high-entropy alloy.

3.3. Constitutive Relation

The J-C model is a classic phenomenological constitutive model that represents the constitutive relationship between stress and strain, strain rate, and temperature during the plastic deformation of materials at high strain rates. The J-C model of materials under uniaxial compression can be expressed as [25]:

$$\sigma = (A + B\varepsilon^n) \left(1 + C \ln \frac{\dot{\varepsilon}_p}{\dot{\varepsilon}_0} \right) [1 - (T^*)^m], \quad (3a)$$

$$T^* = \frac{T - T_r}{T_m - T_r}, \quad (3b)$$

where A , B , and n are strain strengthening coefficients; ε is the equivalent plastic strain; C is strain rate sensitivity coefficient; $\dot{\varepsilon}_p$ is the strain rate; $\dot{\varepsilon}_0$ is the reference strain rate ($\dot{\varepsilon}_0 = 10^{-3} \text{ s}^{-1}$); m is temperature-softening coefficient; T^* is temperature-softening effect; T is the absolute temperature; T_r is room temperature ($T_r = 298 \text{ K}$); and T_m is the melting point of the sample ($T_m = 298 \text{ K}$).

However, the J-C model fails to account for the temperature elevation resulting from plastic deformation. The deformation at high strain rates occurs rapidly, resembling an adiabatic process in which plastic work is transformed into thermal energy, resulting in a rise in the specimen's temperature. Due to thermal softening, this temperature rise significantly influences the constitutive behavior of the material and cannot be disregarded. The distinction in the compressive failure strain between static and dynamic loading is precisely exemplified by the data presented in Figure 6. Considering that a fraction of

plastic deformation is converted into thermal energy, the temperature increase associated with plastic deformation can be directly determined from the constitutive equation. The work-to-heat conversion coefficient for most metals is commonly assumed to be 0.9 [26], and the formula for adiabatic temperature rise can be expressed as [27]:

$$\Delta T = \frac{\beta}{\rho C_p} \int_0^\epsilon \sigma d\epsilon = \frac{0.9}{\rho C_p} \int_0^\epsilon \sigma d\epsilon, \quad (4)$$

where C_p is the specific heat capacity of the material at constant pressure (J/g · K); ρ is the density of the material ($\rho = 10.98 \text{ g/cm}^3$); β is the conversion rate of work to heat ($\beta = 0.9$); and $\int_0^\epsilon \sigma d\epsilon$ is the energy density of the material during deformation.

Substituting the σ value in Formula (3a) into (4), we obtained the solution:

$$\int_{T_0^*}^{T^*} \frac{dT^*}{1 - T^{*m}} = \frac{0.9 \left(1 + C \ln \frac{\dot{\epsilon}_p}{\dot{\epsilon}_0}\right)}{\rho C_p (T_m - T_r)} \int_0^\epsilon (A + B\epsilon^n) d\epsilon, \quad (5)$$

Johnson and Cook tested a large number of materials and deduced that $m \cong 1$. Thus,

$$T^* = 1 - \exp \left[-\frac{0.9 \left(1 + C \ln \frac{\dot{\epsilon}_p}{\dot{\epsilon}_0}\right)}{\rho C_p (T_m - T_r)} \left(A\epsilon + \frac{B\epsilon^{n+1}}{n+1} \right) \right], \quad (6)$$

Substituting Formula (6) into Formula (3a) to obtain the modified J-C constitutive model:

$$\sigma = (A + B\epsilon^n) \left(1 + C \ln \frac{\dot{\epsilon}_p}{\dot{\epsilon}_0}\right) \exp \left[-\frac{0.9 \left(1 + C \ln \frac{\dot{\epsilon}_p}{\dot{\epsilon}_0}\right)}{\rho C_p (T_m - T_r)} \left(A\epsilon + \frac{B\epsilon^{n+1}}{n+1} \right) \right], \quad (7)$$

Substituting the experimental data from Figure 6 into Formula (7) for fitting, the modified J-C constitutive relationship of Nb₁₇Zr₃₃Ti₁₇W₃₃ high-entropy alloy was obtained, and the final expression is as follows:

$$\sigma = (965 + 55.37\epsilon^{0.84}) \left(1 + 0.04 \ln \frac{\dot{\epsilon}_p}{\dot{\epsilon}_0}\right) \exp \left[-\frac{0.9 \left(1 + 0.04 \ln \frac{\dot{\epsilon}_p}{\dot{\epsilon}_0}\right)}{\rho C_p (T_m - T_r)} (965\epsilon + 30.09\epsilon^{1.84}) \right] \quad (8)$$

Figure 8a illustrates the comparison between the experimental flow characteristics at different strain rates and the modified J-C model's calculation results under dynamic compression. Figure 8a demonstrates a strong agreement between the predicted flow characteristics and the experimental curve across various strain rates. As shown in Figure 8b, when the strain rate is 3689 and 4294 s⁻¹, the deformation temperature rise (ΔT) calculated by Formula (4) reaches 279.62 K and 250.04 K, respectively. Strictly speaking, the temperature rise distribution in the material is uneven, but the temperature rise amplitude caused by rapidly moving dislocations may be consistent with the average temperature rise amplitude predicted by the macroscopic model [28]. Based on this consideration, this article assumed that the heat converted from plastic work during deformation causes a uniform temperature rise in the alloy during dynamic loading. The above practice indicates that the improved J-C model can macroscopically predict the flow behavior of materials during a high strain-rate deformation by introducing an average temperature rise.

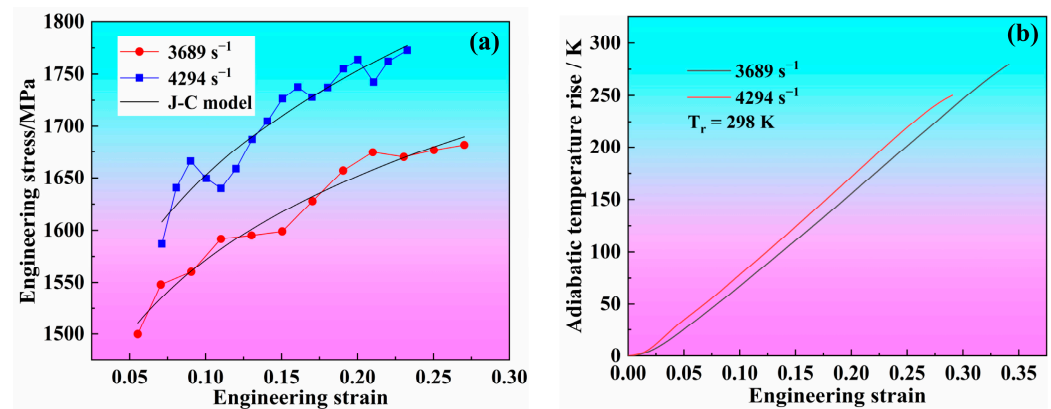


Figure 8. (a) Comparison between dynamic flow stresses and the J-C model for the Nb₁₇Zr₃₃Ti₁₇W₃₃ high-entropy alloy. (b) Variation in the adiabatic temperature rise with the engineering strain at the strain rates of 3689 s⁻¹ and 4294 s⁻¹.

3.4. Failure and Energy Release Mechanism

The phenomenon of energy release resulting from alloy specimen failure during the dynamic compression process was captured by the high-speed camera, as depicted in Figure 9. The experiment captured four sequential frames of images both before and after the moment of specimen failure, where the horizontal axis denotes time and the vertical axis represents the strain rate for two distinct failure tests. The moment at which the appearance of sparks was initially observed was designated as time zero. Figure 9a illustrates the frame preceding the release of energy ($t = -100 \mu\text{s}$). Currently, the SHPB compression rod remains unloaded, and the impact system is in a static state, allowing for a clear observation of the sample's condition through the acrylic tube. The first observation of the energy release phenomenon ($t = 0 \mu\text{s}$) is depicted in Figure 9b, where sparks are observed to propagate within a limited range. The deformation energy stored in the fracture is instantaneously released upon material failure, resulting in localized material heating and melting. Simultaneously, an unbalanced stress at the sample's end causes collision between the hard alloy and the sample, leading to the generation of small material debris. The phenomenon of spark splashing is attributed to the detachment of molten droplets and debris from the block sample, followed by an oxidation reaction with atmospheric oxygen. The oxidation states of various elements on the surface of fragments were analyzed using XPS, as depicted in Figure 10. The peaks corresponding to W 4f, Zr 3d, Nb 3d, Ti 2p, and O 1s were observed at the binding energies of 30.089, 182.089, 203.089, 458.889, and 532.189 eV, respectively, with mass concentration percentages of approximately W (10.99%), Zr (35.84%), Nb (5.56%), Ti (2.96%), and O (31.77%). The XPS data indicate that an oxidation reaction occurred during the impact process, resulting in the formation of predominantly Zr-based oxides, which substantiates the aforementioned phenomenon of energy release. Figure 9c shows the frame after observing the energy release phenomenon ($t = 100 \mu\text{s}$), where the spark range and brightness are significantly greater than the previous frame. This phenomenon arises from the significant impact, which propels the sample fragments to disperse, thereby inducing vigorous chemical reactions and facilitating the enhanced release of chemical energy upon complete exposure to atmospheric oxygen. As demonstrated by high-speed photography in Figure 9d ($t = 200 \mu\text{s}$), the strain rate of 4294 s⁻¹ exhibits the most pronounced energy release reaction, a brilliant light emission with the longest duration. The brightness is visible and disappears at $t = 30 \text{ s}$. At the strain rate of 3689 s⁻¹, only sparks radiate, reducing the range of fire and lasting for a short time (disappearing at $t = 22 \text{ s}$). Figure 9e shows the state of the material after the compression test, with a fracture surface at an angle of approximately 45° to the direction of load loading, indicating that the deformation and fracture direction of the material are the same as the direction of the maximum shear stress. The oxidation reaction and energy release of the Nb₁₇Zr₃₃Ti₁₇W₃₃ high-entropy alloy during high-speed impact can be inferred from Figures 9 and 10. The

severity of the energy release effect during material failure is directly proportional to the strain rate within the experimental range.

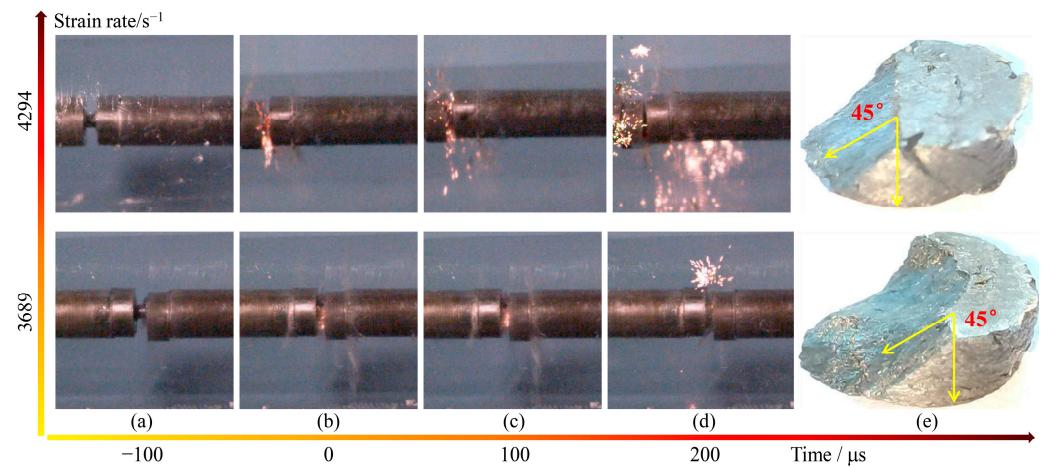


Figure 9. High-speed photography of the sample failure and energy release process.

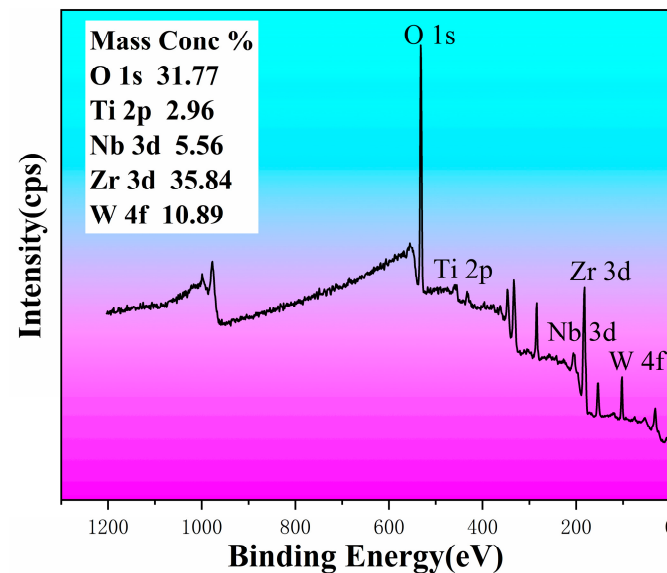


Figure 10. XPS spectra of the Nb₁₇Zr₃₃Ti₁₇W₃₃ impact fragments.

The Nb₁₇Zr₃₃Ti₁₇W₃₃ high-entropy alloy demonstrates a pronounced strain rate hardening behavior under both quasi-static and dynamic conditions, as depicted in Figure 6. Moreover, it exhibits exceptional strong plastic bonding characteristics when subjected to high-speed loading. In order to investigate the potential microscopic deformation mechanism, it is imperative to conduct further SEM analysis on the failure samples. Figure 11 illustrates the morphology of the dynamic compression fracture. A significant number of dimples can be observed on the fracture surface (Figure 11c), indicating the occurrence of localized plastic deformation during material fracturing. During the dynamic fracture of the Nb₁₇Zr₃₃Ti₁₇W₃₃ high-entropy alloy, the strain energy accumulated in the localized shear band is dissipated as heat, resulting in elevated temperatures at the fracture surface. This localized heating induces plastic deformation and facilitates the formation of dimples during sample failure. The elongation of the dimples along the compression direction, as depicted in Figure 11d, with a size on the order of tens of nanometers, signifies excellent plasticity exhibited by the alloy under dynamic compression. The presence of shear slip marks in Figure 11e serves as a precursor to crack initiation and material failure, indicating the occurrence of a significant slip along the direction of maximum shear force during

compression, ultimately leading to fracture failure. This finding is consistent with the observed macroscopic fracture surface displaying a 45° angle (Figure 11a). Figure 11f shows evidence of melting traces, indicating that the alloy undergoes severe fragmentation under high-speed impact loading to facilitate plastic deformation absorption. Due to the inadequate dissipation of the high temperature generated upon impact, there are indications of ‘molten droplets’ on the fracture surface of the alloy.

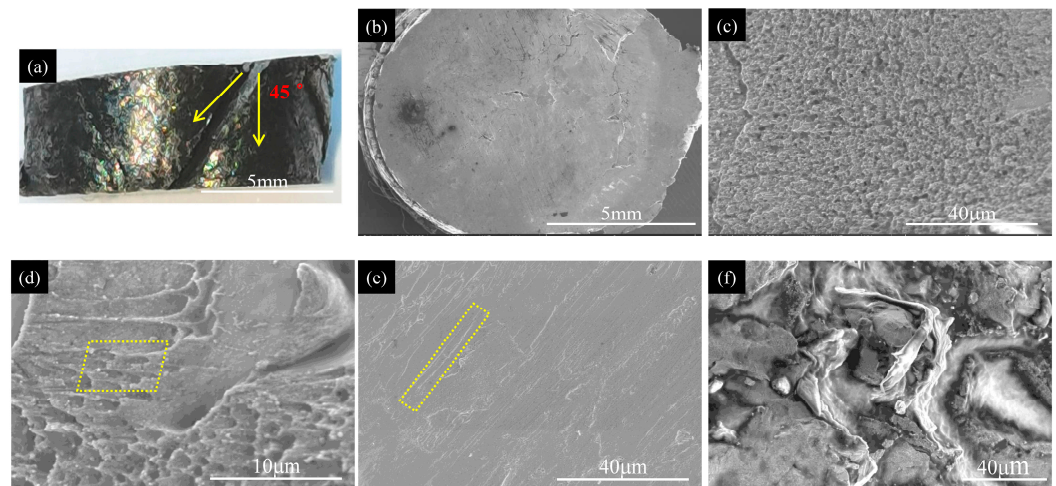


Figure 11. Dynamic compression fracture morphology of the $\text{Nb}_{17}\text{Zr}_{33}\text{Ti}_{17}\text{W}_{33}$ high-entropy alloy: (a) axial small-scale diagram; (b) radial small-scale diagram; (c) dimples; (d) elongated dimples; (e) shear slip line; and (f) melting marks.

4. Conclusions

Energetic structural materials should exhibit optimal performance under high-speed deformation conditions, such as explosion, penetration, or high-velocity impact. These materials must possess exceptional dynamic properties to effectively meet the demands of their intended applications. Therefore, investigating the deformation behavior and fracture mechanism of high-entropy alloys under dynamic loading conditions holds significant guiding implications for further exploring the application potential of high-entropy alloys in the field of energetic materials.

The research findings suggest that the $\text{Nb}_{17}\text{Zr}_{33}\text{Ti}_{17}\text{W}_{33}$ alloy demonstrates a pronounced positive strain-rate strengthening effect, with both the yield strength and fracture limit of the material increasing as the strain rate increases. Furthermore, compared to quasi-static loading conditions, the alloy exhibits enhanced strain rate sensitivity under dynamic loads. The $\text{Nb}_{17}\text{Zr}_{33}\text{Ti}_{17}\text{W}_{33}$ high-entropy alloy with a dual-phase structure demonstrates exceptional strength and plasticity, particularly at a loading rate of 4294 s^{-1} , exhibiting a yield strength of 1587 MPa, fracture strength of 1772 MPa, and fracture strain approaching 25%. During high-speed impact, the sample undergoes fragmentation, triggering chemical reactions and a violent release of energy. This alloy exhibits significant potential for use in extreme load-bearing applications, such as high-performance warhead materials.

The analysis reveals that the material exhibits a macroscopic ductile fracture, with a significant presence of elongated dimples observed on the fracture surface. During the compression fracture failure process of the sample, strain energy is released and oxidation reactions occur, resulting in the dispersion of sparks. With an increase in the strain rate, there is a corresponding escalation in material fragmentation, leading to a more pronounced manifestation of energy release at the moment of failure. ‘Melt droplets’ are observable on the fracture surface, which is inclined at a 45° angle toward the direction of loading. Shear slip marks within the fracture surface indicate that the alloy fractured in a shear mode, suggesting potential for exhibiting a self-sharpening behavior.

Considering the influence of the adiabatic temperature rise on dynamic compression, a modified Johnson–Cook model was employed to describe the plastic rheological behavior

of the Nb₁₇Zr₃₃Ti₁₇W₃₃ high-entropy alloy under dynamic constitutive conditions. The obtained constitutive equation effectively captured the plastic rheological behavior of high-entropy alloys at high strain rates, with the predicted flow characteristics demonstrating excellent agreement with the experimental curves, thus confirming the efficacy of the proposed model.

Author Contributions: Conceptualization, W.J. and Q.Z.; methodology, W.J.; validation, X.Y.; writing—original draft preparation, W.J.; writing—review and editing, W.J. and Z.Z. All authors have read and agreed to the published version of the manuscript.

Funding: This research received no external funding.

Data Availability Statement: The data presented in this study are available upon request from the corresponding author. The data are not publicly available due to privacy.

Conflicts of Interest: The authors declare no conflict of interest.

Dual-Use Research Statement

We have made the following statements to our paper titled “Dynamic Mechanical Behavior and Energy Release Effect of a Novel Nb₁₇Zr₃₃Ti₁₇W₃₃ High-Entropy Alloy under Impact Load”.

Ø Explanation of Potential Risks: Our paper examines the mechanical behavior and energy release effect of a novel Nb₁₇Zr₃₃Ti₁₇W₃₃. The research is limited to providing some theoretical and experimental support for the development of impact dynamics only and does not pose a threat to public health or national security.

Ø Evaluation of Benefits to the General Public: Our research is limited to the academic field, which is beneficial to the development of material science. There is no risk to the general public.

Ø Compliance with Laws: As an ethical responsibility, we strictly adhere to relevant national and international laws about dual-use research. And we have considered and adhered to these regulations in our paper.

References

1. Macdonald, B.E.; Fu, Z.; Zheng, B. Recent progress in high entropy alloy research. *JOM* **2017**, *69*, 2024–2031. [[CrossRef](#)]
2. Li, Z.Z.; Zhao, S.T.; Ritchie, R.O. Mechanical properties of high-entropy alloys with emphasis on face-centered cubic alloys. *Prog. Mater. Sci.* **2019**, *102*, 296–345. [[CrossRef](#)]
3. Kumar, N.; Subramaniam, A. Orientational high-entropy alloys. *Philos. Mag. Lett.* **2014**, *94*, 750–754. [[CrossRef](#)]
4. Yang, X.W.; Shi, X.H.; Yang, H.J. Entropy versus enthalpy in hexagonal-close-packed highentropy alloys. *Rare Met.* **2022**, *41*, 2906–2920. [[CrossRef](#)]
5. Otto, F.; Dlouhý, A.; Somsen, C.; Bei, H.; Eggeler, G.; George, E.P. The influences of temperature and microstructure on the tensile properties of a CoCrFeMnNi high-entropy alloy. *Acta Mater.* **2013**, *61*, 5743–5755. [[CrossRef](#)]
6. Chuang, M.H.; Tsai, M.H.; Wang, W.R. Microstructure and wear behavior of Al_xCo_{1.5}CrFeNi_{1.5}Ti_y high-entropy alloys. *Acta Mater.* **2011**, *59*, 6308–6317. [[CrossRef](#)]
7. Miracle, D.B.; Senkov, O.N. A critical review of high entropy alloys and related concepts. *Acta Mater.* **2017**, *122*, 448–511. [[CrossRef](#)]
8. Senkov, O.N.; Wilks, G.B.; Miracle, D.B. Refractory high-entropy alloys. *Intermetallics* **2010**, *18*, 1758–1765. [[CrossRef](#)]
9. Li, C.W.; Ma, Y.; Yang, X. New TiTaNbZrMo high-entropy alloys for metallic biomaterials. *Mater. Res. Express* **2021**, *8*, 105403. [[CrossRef](#)]
10. Senkov, O.N.; Wilks, G.B.; Scott, J.M. Mechanical properties of Nb₂₅Mo₂₅Ta₂₅W₂₅ and V₂₀Nb₂₀Mo₂₀Ta₂₀W₂₀ refractory high entropy alloys. *Intermetallics* **2011**, *19*, 698–706. [[CrossRef](#)]
11. Zou, Y.; Ma, H.; Spolenak, R. Ultrastrong ductile and stable high-entropy alloys at small scales. *Nat. Commun.* **2015**, *6*, 7748. [[CrossRef](#)] [[PubMed](#)]
12. He, H.T.; Fang, J.X.; Wang, J.X.; Sun, T.; Yang, Z.; Ma, B.; Chen, H.T.; Wen, M. Carbide-reinforced Re_{0.1}Hf_{0.25}NbTaW_{0.4} refractory high-entropy alloy with excellent room and elevated temperature mechanical properties. *Int. J. Refract. Met. Hard Mat.* **2023**, *116*, 106349. [[CrossRef](#)]
13. Guo, Q.W.; Hou, H.; Pan, Y.; Pei, X.L.; Song, Z.; Peter, K.L.; Zhao, Y.H. Hardening-softening of Al_{0.3}CoCrFeNi high-entropy alloy under nanoindentation. *Mater. Des.* **2023**, *231*, 112050. [[CrossRef](#)]

14. Ma, S.G.; Jiao, Z.M.; Qiao, J.W.; Yang, H.J.; Zhang, Y.; Wang, Z.H. Strain rate effects on the dynamic mechanical properties of the AlCrCuFeNi₂ high-entropy alloy. *Mater. Sci. Eng. A* **2016**, *649*, 35–38. [[CrossRef](#)]
15. Li, Z.; Zhao, S.; Diao, H. High-velocity deformation of Al_{0.3}CoCrFeNi high-entropy alloy: Remarkable resistance to shear failure. *Sci. Rep.* **2017**, *7*, 42742. [[CrossRef](#)]
16. Shen, Z.D.; Ma, Z.L.; Xu, Z.Q. Grain refinement and abnormal peritectic solidification in WxNbTiZr high-entropy alloys. *Mater. Des.* **2022**, *224*, 111381. [[CrossRef](#)]
17. Wang, R.X. Microstructure Evolution and Energetic Structural Properties of NbZrTiTa High-Entropy Alloy. Master's Thesis, National University of Defense Technology, Changsha, China, 2018.
18. Dehgahi, S.; Alaghmandfard, R.; Tallon, J.; Odeshi, A. Microstructural evolution and high strain rate compressive behavior of as-built and heat-treated additively manufactured maraging steels. *Mater. Sci. Eng. A Struct. Mater. Prop. Microstruct. Process.* **2021**, *815*, 141183. [[CrossRef](#)]
19. Weaver, J.S.; Livescu, V.; Mara, N.A. A comparison of adiabatic shear bands in wrought and additively manufactured 316L stainless steel using nanoindentation and electron backscatter diffraction. *J. Mater. Sci.* **2020**, *55*, 1738–1752. [[CrossRef](#)]
20. Li, J.G.; Li, Y.L.; Suo, T. Numerical simulations of adiabatic shear localization in textured FCC metal based on crystal plasticity finite element method. *Mater. Sci. Eng. A Struct. Mater. Prop. Microstruct. Process.* **2018**, *737*, 348–363. [[CrossRef](#)]
21. Lee, W.S.; Liu, C.Y.; Sun, T.N. Dynamic impact response and microstructural evolution of inconel 690 superalloy at elevated temperatures. *Int. J. Impact Eng.* **2005**, *32*, 210–223. [[CrossRef](#)]
22. Hosson, J.T.M.D.; Roos, A.; Metselaar, E.D. Temperature rise due to fast-moving dislocations. *Philos. Mag. A* **2001**, *81*, 1099. [[CrossRef](#)]
23. Zou, L.X.; Sun, Y.; Qi, L.Z. Influence of Preheating and Annealing on the Reaction Kinetics of Uranium and Uranium-Niobium Alloys with Hydrogen Gas. *J. Nucl. Radiochem.* **2004**, *26*, 153–157.
24. Cheng, Q.S.; Han, P.D.; Wu, X.L. Effect of short-time annealing on work hardening of low steel with nano lamellar structure. *Heat Treat. Met.* **2018**, *43*, 182–186.
25. Wang, L.; Qiao, J.W.; Ma, S.G.; Jiao, Z.M.; Zhang, T.W.; Chen, G.; Zhao, D.; Zhang, Y.; Wang, Z.H. Mechanical response and deformation behavior of Al_{0.6}CoCrFeNi high-entropy alloys upon dynamic loading. *Mater. Sci. Eng. A* **2018**, *727*, 208–213. [[CrossRef](#)]
26. Wang, L. Dynamic Mechanical Properties of CoCrFeNiAl_x High Entropy Alloys. Master's Thesis, Taiyuan University of Technology, Taiyuan, China, 2018.
27. Zener, C.; Hollomon, J.H. Effect of Strain Rate upon Plastic Flow of Steel. *J. Appl. Phys.* **1944**, *15*, 22–32. [[CrossRef](#)]
28. Cheng, J.; Sia, N.-N.; Guo, W. A unified constitutive model for strain-rate and temperature dependent behavior of molybdenum. *Mech. Mater.* **2001**, *33*, 603–616. [[CrossRef](#)]

Disclaimer/Publisher's Note: The statements, opinions and data contained in all publications are solely those of the individual author(s) and contributor(s) and not of MDPI and/or the editor(s). MDPI and/or the editor(s) disclaim responsibility for any injury to people or property resulting from any ideas, methods, instructions or products referred to in the content.